

ACID RAIN: MESOSCALE MODEL

By Hsiao-ming Hsu*

INTRODUCTION

A mesoscale numerical model of the Florida peninsula has been formulated and applied to a dry, neutral atmosphere. The preliminary results of this model presented in this paper are very encouraging. To simulate synoptically undisturbed and disturbed situations in this area, several modifications have appeared desirable; thus, a new model quite different from the one just mentioned has evolved. A submesoscale model for the Cape Canaveral area will use the results from the mesoscale model as continuous inputs. The prospective use of the Control Data Corporation (CDC) STAR-100 computer at the NASA Langley Research Center for the submesoscale model is discussed.

PRELIMINARY RESULTS

The numerical model presented in reference 1 is tested under synoptically undisturbed conditions. Because this test is for demonstrating the simulation of only the basic dynamics in the mesoscale region and for detecting any programming error in the model, three assumptions are applied to simplify the calculation.

1. The atmosphere is assumed to be dry; i.e., the parameterization of cloud and precipitation physics is not yet included.
2. A constant potential temperature ($\theta = 298.16$ K) and a constant geostrophic windspeed ($V = 6$ m/sec) are assigned to the model as the initial conditions.
3. The daytime land surface temperature is represented by a single sine function that limits the maximum heating to 10 K at the end of the sixth hour of simulation. The water surface is assigned a constant temperature that is the same as the initial temperature of the land surface. (The time step is 5 minutes.)

Two cases, differing only in the direction of the prevailing geostrophic wind, are examined: a prevailing southwest wind and a prevailing southeast wind, both 6 m/sec at all levels initially.

*University of Michigan.

Prevailing Southwest Wind

Results from the simulation experiment of prevailing southwest wind are shown for the various levels and times in figures 1 to 3. The horizontal wind field at the 50-meter level shows only a slight change from the prevailing wind at the end of 2 hours (figs. 1(a) and 1(b)). By the third hour (fig. 1(c)), the low-level wind direction has turned noticeably at the shorelines and especially sharply along the east coast of the Florida peninsula. A definite low-level convergence zone is formed by the end of the fourth hour of simulation (fig. 1(d)). The sea-breeze convergence zone continues to develop and moves inland during the fifth (fig. 1(e)) and sixth (fig. 1(f)) hours.

The horizontal wind fields at 200-, 450-, 800-, and 1250-meter levels are shown at the end of the sixth hour in figure 2. The change of wind from 50 to 1250 meters reveals the vertical sea-breeze circulation along the east coast: the sea breeze gives onshore winds in the lower levels and offshore winds in the higher levels. The gradual veering of the wind from southeast or east near the surface to southwest aloft is clearly shown.

Figure 3 gives the computed horizontal distributions of vertical velocity at 1250 meters at the end of each hour of simulation. The velocity fields are mainly developed by the effects of advection over the gradually warmed peninsula. The convergence zone forms first along the west coast, whereas divergence prevails along the east coast. By the third hour, convergence is also noted along the east coast. Several distinct maximums of positive vertical velocity exist along the east coast at the sixth model hour. The maximum south of Lake Okeechobee, predicted by Pielke (ref. 2), has the greatest upward velocity. Two other maximums north of Lake Okeechobee, although weaker than the one just mentioned, are very close to the area of Cape Canaveral. Pielke has demonstrated that the predicted regions of positive vertical velocity agree qualitatively with radar and satellite observations of cloud and shower activity over southern Florida on undisturbed days. His study did not, however, extend north of Lake Okeechobee and so did not reveal the effects at Cape Canaveral. The maximums of positive upward motion in the author's results are expected to be closely related to cloud and shower activity, at least qualitatively. In this case, having the southwest wind in a synoptically undisturbed situation, disturbed weather contributed solely by the sea-breeze convergence appears both in the Cape Canaveral area and in southeastern Florida.

Prevailing Southeast Wind

The horizontal wind patterns for prevailing southeast wind at the 50-meter level are shown in figure 4 for the end of each model hour. Again, a slight turning is seen at the coastlines by the end of the second hour (fig. 4(b)). The convergence zone develops gradually along the west coast of Florida. At the sixth hour, the horizontal wind distributions at heights of 200, 450, 800, and 1250 meters indicate the sea-breeze circulation along the west coast (fig. 5). The vertical velocity fields at the 1250-meter level at the end of each model hour (fig. 6) show the evolution of the sea-breeze

convergence zone. Under the southeast wind regime, the area of Cape Canaveral is covered by a field of downward vertical velocity after the second hour (fig. 6(b)), but a band of upward motion that occurs inland during the fifth and sixth hours (figs. 6(e) and 6(f), respectively) indicates possible weather disturbance. Along the western shore of Florida, however, the vertical velocity fields are more strongly developed.

For both cases, the motion fields appear to be somewhat exaggerated after 5 hours of simulation. This result is a product of the highly idealized assumption that the atmosphere is adiabatic (constant potential temperature $\theta = 298.16$ K) initially. The computations are stopped at the end of the sixth hour.

Discussion

Analogous features are shown under the two different prevailing wind directions. They are not caused by different dynamics but by the orientation of the Florida peninsula with respect to the wind. On synoptically undisturbed days, the local weather is dominated by the sea breeze. For the Cape Canaveral area, locally disturbed weather can be expected to appear under a general southwest flow. Under a general southeast flow, disturbances at the Cape are not expected, but they might develop inland and downwind from the Cape. This conclusion agrees qualitatively with Neumann's report that the probability of having afternoon thunderstorms under southeast winds is low but that the probability of having them under southwest winds in the summer months at the Cape is more than 50 percent (ref. 3).

Comparison of the author's results with those of Pielke (ref. 2) reveals that the strength of upward motion is weaker in the author's simulation than in Pielke's before the end of the fifth hour. Because the author's horizontal grid spacing is about three times longer than Pielke's, the extremes shown by Pielke's model are necessarily greater than those shown by the author's. At the same time, the author's model is flexible in that the grid spacing can be adjusted in both the horizontal and vertical directions. The question of increased resolution of the model in turn raises the question of the limits of computer capacity. The author proposes, as a second stage of model development, the introduction of a cloud-scale model (grid spacing 2 by 2 by 0.5 kilometers) the initial and boundary conditions of which will be derived from the mesoscale model.

Although it is clear that the modeled mesoscale dynamic processes do predict the sea-breeze regimes along the Florida coasts, it is also clear that important modifications must be introduced to achieve more complete simulations. These are presented and discussed in the following section.

RECENT DEVELOPMENTS

To generate more complete mesoscale information over the region of the Florida peninsula, the following additional considerations are introduced.

Parameterization of Convective Cloud and Precipitation

The study of parameterization described in the section entitled "Future Work" leads to the conclusion that Kuo's method (ref. 4) is the best approach for meeting the requirements of fidelity with simplicity. This parameterization is recommended partly by its more rigorous derivation and partly by its potential for further development. It will, for example, enable the use of a convective cloud model to obtain values for the cloud temperature and specific humidity.

The parameterization allows for two kinds of moisture sources for a convective cloud (fig. 7). One is the net convergence of moisture between cloud base and cloud top

$$- \int_{z_b}^{z_t} t \left[\frac{\partial}{\partial x} (\rho q u) + \frac{\partial}{\partial y} (\rho q v) + \frac{\partial}{\partial z} (\rho q w) \right] dz$$

and the other is the evaporation between the surface and cloud base

$$\rho_{z_b} C_D V_{z_b} (q_g - q_{z_b})$$

Then, the total moisture available to the air column in the convective cloud is

$$M = - \int_{z_b}^{z_t} t \left[\frac{\partial}{\partial x} (\rho q u) + \frac{\partial}{\partial y} (\rho q v) + \frac{\partial}{\partial z} (\rho q w) \right] dz + \rho_{z_b} C_D V_{z_b} (q_g - q_{z_b}) \quad (1)$$

where z_t and z_b are the heights of cloud top and cloud base, respectively; u and v are the x - and y -component velocities; w is vertical velocity; q is the specific humidity; ρ is density; C_D is the drag coefficient; V is the horizontal windspeed; and g denotes the surface.

The total moisture available M may fuel the convective cloud by becoming entrained through the cloud sides, by pumping moisture through the cloud base,

or by evaporating part of M in the environment. Two kinds of sink from a convective cloud are parameterized: the evaporation from cloud sides and the precipitation received at the surface. The evaporation both in the environment and from cloud sides represents moisture input to the air column βM . The precipitation received at the surface represents the removal of moisture $(1 - \beta)M$ from the air column. The processes within the dashed box in figure 7 are the subgrid processes in the author's mesoscale model and are not evaluated explicitly.

The source term for the potential temperature θ can be expressed by

$$S_{\theta 2} = \frac{L}{\pi} C \quad (2)$$

where L is the latent heat of evaporation and C is the precipitation rate produced by a convective cloud. The value π is the scaled pressure

$$\pi = c_p \left(\frac{p}{p_0} \right)^{\frac{R}{C}} \quad (3)$$

where c_p is the specific heat at constant pressure, R is the gas constant for dry air, p is the pressure, and $p_0 = 1000$ millibars is a reference pressure.

The vertically integrated precipitation rate gives the total amount of precipitation.

$$\int_{z_b}^{z_t} \rho C dz = (1 - \beta)M \quad (4)$$

The precipitation rate produced by a convective cloud may be written as

$$\rho C = (1 - \beta)M \frac{N(z)}{(z_t - z_b)} \quad (5)$$

if the vertical distribution function $N(z)$ of θ satisfies

$$\int_{z_b}^{z_t} N(z) dz = z_t - z_b \quad (6)$$

Supposing that $N(z)$ is represented as a function of the difference of potential temperatures between the cloud interior and its environment,

$$N(z) = \frac{(\theta_c - \theta)}{<\theta_c - \theta>} \quad (7)$$

where

$$<\theta_c - \theta> = \frac{1}{(z_t - z_b)} \int_{z_b}^{z_t} (\theta_c - \theta) dz \quad (8)$$

Then,

$$C = \frac{(1 - \beta)M}{\rho(z_t - z_b)} \frac{(\theta_c - \theta)}{<\theta_c - \theta>} \quad (9)$$

where the subscript c denotes cloud.

Substituting equation (9) into equation (2) gives

$$S_{\theta 2} = \frac{L(1 - \beta)M}{\pi \rho (z_t - z_b)} \frac{(\theta_c - \theta)}{<\theta_c - \theta>} \quad (10)$$

for the source term for θ . Similarly, the source term for q is

$$S_{q2} = - \frac{(1 - \beta)M}{\rho(z_t - z_b)} \frac{(\theta_c - \theta)}{\langle \theta_c - \theta \rangle} \quad (11)$$

The coefficient β representing the fraction of M remaining in the air column is a very important and crucial factor. The whole evaporation process is controlled by β . It has been assumed to have the following form (ref. 5).

$$\beta = \begin{cases} \left[\frac{1 - \overline{q/q_s}}{1 - \overline{q/q_s}^*} \right]^n, & \text{when } \overline{q/q_s} \geq \overline{q/q_s}^* \\ 1, & \text{when } \overline{q/q_s} < \overline{q/q_s}^* \end{cases} \quad (12)$$

where the subscript $*$ represents a critical value to be specified and the superscript n is a constant.

The cloud variables that have the subscript c are determined by the saturated adiabat between cloud base and cloud top. It is intended that these values will eventually be computed by using a convective cloud model.

Diagnostic Vertical Velocity Equation

It is intended to represent all diurnal, seasonal, and synoptic characteristics of the region of interest. A shallow model clearly does not meet this requirement. To account for deep convection, the model is extended to 16 kilometers vertically in 18 levels (table I). The assumption of constant density can no longer be used and must be replaced by the complete continuity equation for a compressible fluid. Finally, a modified Richardson's equation is used to calculate the vertical velocity diagnostically.

The principle of mass conservation gives the continuity equation in three dimensions.

$$\nabla \cdot \vec{V} = - \frac{1}{\rho} \frac{d\rho}{dt} \quad (13)$$

where

$$\nabla = \frac{\partial}{\partial x} \vec{i} + \frac{\partial}{\partial y} \vec{j} + \frac{\partial}{\partial z} \vec{k}$$

$$\vec{V} = u\vec{i} + v\vec{j} + w\vec{k}$$

and

$$\frac{d}{dt} = \frac{\partial}{\partial t} + \vec{V} \cdot \nabla$$

Taking the logarithm of the equation of state and the definitions of π and θ yields

$$\ln p = \ln \rho + \ln R + \ln T \quad (14)$$

$$\ln \pi = \ln c_p + R/c_p \ln p - R/c_p \ln p_0 \quad (15)$$

$$\ln \theta = \ln T - \ln \pi + \ln c_p \quad (16)$$

where T is the temperature. Differentiating equations (14), (15), and (16) and making substitutions, one obtains

$$\frac{1}{\rho} \frac{d\rho}{dt} = \frac{c_v}{R} \frac{1}{\pi} \frac{d\pi}{dt} - \frac{1}{\theta} \frac{d\theta}{dt} \quad (17)$$

where c_v is the specific heat at constant volume. Substitution of equation (17) into equation (13) gives

$$\nabla \cdot \vec{V} = - \frac{c_v}{R} \frac{1}{\pi} \frac{d\pi}{dt} + \frac{1}{\theta} \frac{d\theta}{dt} \quad (18)$$

Multiplying p/π on each side of equation (18), taking $\vec{V} \cdot \nabla \pi$ in $d\pi/dt$ from the right-hand side of equation (18) to the left-hand side, and rearranging terms, one has

$$\nabla \cdot \left(\frac{p}{\pi} \vec{V} \right) = - \frac{c}{R} \frac{p}{\pi^2} \frac{\partial \pi}{\partial t} + \frac{p}{\pi \theta} \frac{d\theta}{dt} \quad (19)$$

The time derivative of the hydrostatic equation

$$\frac{\partial}{\partial t} \left(\frac{\partial \pi}{\partial z} \right) = \frac{\partial}{\partial t} \left(- \frac{g}{\theta_v} \right) \quad (20)$$

is integrated from any level z to the model top H to determine $\partial \pi / \partial t$.

$$\frac{\partial \pi}{\partial t} = A + B \quad (21)$$

where

$$A = \left. \frac{\partial \pi}{\partial t} \right|_H \quad (22)$$

$$B = g \int_z^H \frac{\partial}{\partial t} \left(\frac{1}{\theta_v} \right) dz \quad (23)$$

and

$$\theta_v = (1 + 0.609q)\theta$$

Both $\partial/\partial t(1/\theta_v)$ and $d\theta/dt$ can be evaluated explicitly from the equations of potential temperature and specific humidity in the model. Then, equation (19) becomes

$$\nabla \cdot \left(\frac{p}{\pi} \vec{V} \right) = - \frac{c_v}{R} \frac{p}{\pi^2} (A + B) + \frac{p}{\pi \theta} \frac{d\theta}{dt} \quad (24)$$

after substituting equation (21) into equation (19).

Integrating equation (24) from the surface to any height z and applying the surface boundary condition for w , $w = 0$ at $z = 0$, one has

$$w = - \frac{\pi}{p} \int_0^z \left[\frac{\partial}{\partial x} \left(\frac{p}{\pi} u \right) + \frac{\partial}{\partial y} \left(\frac{p}{\pi} v \right) \right] dz - \frac{\pi}{p} \int_0^z \left[\frac{c_v}{R} \frac{p}{\pi^2} (A + B) - \frac{p}{\pi \theta} \frac{d\theta}{dt} \right] dz \quad (25)$$

This equation gives the values of the vertical velocity at any point and is called the "modified" Richardson's equation.

If the top boundary condition for w , $w = 0$ at $z = H$, is further applied, the pressure tendency will be given as follows.

$$\left. \frac{\partial \pi}{\partial t} \right|_H = A$$

$$= \frac{- \int_0^H \left[\frac{\partial}{\partial x} \left(\frac{p}{\pi} u \right) + \frac{\partial}{\partial y} \left(\frac{p}{\pi} v \right) + \frac{c_v}{R} \frac{p}{\pi^2} B - \frac{p}{\pi \theta} \frac{d\theta}{dt} \right] dz}{\frac{c_v}{R} \int_0^H \frac{p}{\pi^2} dz} \quad (26)$$

The pressure is adjusted by the predicted value from equation (26) at the model top, and the rest of the π -field is calculated from the hydrostatic equation.

Lateral and Upper Boundary Conditions

The Neumann-type lateral boundary condition gives some noise along the boundaries. It can be found in figures 3 and 6. The amplitude of this noise is small, but the noise will be amplified in a stably stratified atmosphere and become fast-moving internal gravity waves. These waves can seriously contaminate the model results. Perkey and Kreitzberg (ref. 6) developed a method to control this problem; this method has been adapted to the present model.

For both lateral and upper boundaries, the variables u , v , θ , and q (represented by D) on the boundary region will be determined by weighting their local tendencies.

$$\frac{\partial D}{\partial t}(I) = w_1(I) \left. \frac{\partial D}{\partial t}(I) \right|_m + \left[1 - w_1(I) \right] \left. \frac{\partial D}{\partial t}(I) \right|_l \quad (27)$$

where the subscripts m and l represent mesoscale and large scale, respectively. The weighting functions for $\partial D/\partial t$ are as follows.

$$\left. \begin{array}{l} w_1(B) = 0.0 \\ w_1(B \pm 1) = 0.3 \\ w_1(B \pm 2) = 0.7 \\ w_1(B \pm 3) = 0.9 \\ w_1(B \pm 4) = 1.0 \end{array} \right\} \quad (28)$$

where B denotes the grid point at the boundary, $B \pm 1$ is the grid point next to B (one grid space in from the boundary), etc.

The vertical velocity w is also determined by means of a weighting procedure as follows.

$$w(I) = w_2(I)w(I) \Big|_m \quad (29)$$

The weighting functions for w are as follows.

$$\left. \begin{array}{l} w_2(B) = 0.00 \\ w_2(B \pm 1) = 0.25 \\ w_2(B \pm 2) = 0.50 \\ w_2(B \pm 3) = 0.75 \\ w_2(B \pm 4) = 1.00 \end{array} \right\} \quad (30)$$

These weighting functions may be adjusted, depending upon test results.

Boundary-Layer Parameterization

To understand the full diurnal variation of mesoscale weather is one of the author's goals. Deardorff's equation (ref. 7) may be used to model the daytime growth of the height of the planetary boundary layer (PBL). The equation is not, however, capable of simulating the variation of the height of the PBL after sunset and before sunrise next morning. To predict the height of the PBL at night, the formulation developed by Smeda (ref. 8) will be used.

$$\frac{\partial H_*}{\partial t} = - \left(u \left|_{H_*} \frac{\partial H_*}{\partial x} + v \left|_{H_*} \frac{\partial H_*}{\partial y} \right. \right) + 0.06 \frac{u_*^2}{H_* f} \left[1 - \left(\frac{3.3 H_* f}{u_*} \right)^3 \right] \quad (31)$$

where $f = 2\Omega \sin \phi$, Ω is the Earth rotation rate, ϕ is the latitude, H_* is the height of the PBL, and u_* is the frictional velocity. The vertical profile of the eddy exchange coefficients remains the same as before.

FUTURE WORK

Improvements of the Mesoscale Model

The mesoscale model is now quite well developed and will be used to provide basic predictive information for the Florida peninsula. As is evident in the model derivations, it has been necessary to idealize and/or parameterize numerous component parts of the problem. It is anticipated that development of techniques and procedures for handling these component parts will continue and that improvements of the model will be made possible by these developments. This is a continuing process which will provide improvement but cannot be expected to achieve perfection in the model.

Development of a Submesoscale Model

To simulate the processes of the solid rocket motor exhaust product removal and the patterns of deposition that they produce in the area of Cape Canaveral after Space Shuttle launches, a submesoscale numerical model is being developed. The model domain is in three dimensions, 90 by 90 by 15 kilometers. The approximate location is shown in figure 8. Processes will be depicted in terms of the behavior of the meteorological variables and model parameters at some 65 596 grid points (a spacing of 2 by 2 by 0.5 kilometers). The basic equations are derived from the theory of atmospheric dynamics and thermodynamics, cloud and precipitation physics, boundary-layer dynamics, and air pollution chemistry. Initial and boundary conditions will be obtained continuously from the output of the mesoscale model.

The requirements of this model in terms of computer capacity and speed are very great. Consequently, a comparative study of the available and soon-to-be available computer facilities has been undertaken.

COMPARATIVE STUDY OF COMPUTER FACILITIES

A brief comparative study of the prominent advanced computer systems that are or may become available has been made. The systems considered are the CDC-6600, the CDC-7600, the Amdahl-470V/6, the CRAY-1, and the STAR-100.

Central processing unit (CPU) rates and memory storage capacities are tabulated and compared in terms of performance ratios in table II. The internal core memory is augmented by virtual memory of unlimited capacity in the Amdahl and the STAR systems. This may be a necessary feature for the submesoscale model.

Clearly, the STAR-100 system is comparable to the CRAY-1 in terms of the CPU rates. The variation of these rates for a given unit is a function of the kind and extent of the computations and tends upward for the array computers as the number of grid points increases. For the STAR-100, in particular, the CPU performance ratio with respect to the CDC-6600 varies as shown in table III.

It is, of course, not valid to extrapolate the trend shown. The anticipated model space of 65 596 grid points will clearly require use of the virtual memory capability of the STAR. At present, no means exists for estimating how the size of the model will affect the overall speed of simulation.

Advantages of the Amdahl-470V/6 at the University of Michigan and of the CRAY-1/CDC-7600 at the National Center for Atmospheric Research (NCAR) are that both have sophisticated graphics facilities and that the CRAY has both scalar and vector registers. It is not yet clear to what extent these features might simplify the procedures and facilitate the presentation of simulation results.

One consideration of significance in selecting the computer facility to be used is that of competing demands for computer times. The NCAR is currently inviting requests for time on the CRAY, and there is little doubt that the atmospheric modeling community will respond. If the STAR is made available on comparable financial terms to the present project, the much more restricted competition for its use will probably make it the more attractive alternative.

REFERENCES

1. Dingle, A. N.: Rain Scavenging of Solid Rocket Exhaust Clouds. NASA CR-2928, 1978.
2. Pielke, R. A.: A Three-Dimensional Numerical Model of the Sea Breezes Over South Florida. *Monthly Weather Rev.*, vol. 102, 1974, pp. 115-139.
3. Neumann, C. J.: Frequency and Duration of Thunderstorms at Cape Kennedy, Part II. *WBTM-SOS-6*, 1970.
4. Kuo, H.-L.: Further Studies of the Parameterization of the Influence of Cumulus Convection on Large-Scale Flow. *J. Atmos. Sci.*, vol. 31, 1974, pp. 1232-1240.
5. Anthes, R. A.: A Cumulus Parameterization Scheme Utilizing a One-Dimensional Cloud Model. *Monthly Weather Rev.*, vol. 105, 1977, pp. 270-286.
6. Perkey, D. J.; and Kreitzberg, C. W.: A Time-Dependent Lateral Boundary Scheme for Limited-Area Primitive Equation Models. *Monthly Weather Rev.*, vol. 104, 1976, pp. 744-755.
7. Deardorff, J. W.: Three-Dimensional Numerical Study of the Height and Mean Structure of a Heated Planetary Boundary Layer. *Boundary Layer Meteorol.*, vol. 7, 1974, pp. 81-106.
8. Smeda, M. S.: Incorporation of Planetary Boundary Layer Processes Into Numerical Forecasting Models. Rep. DM-23, Univ. of Stockholm, 1977.

TABLE I.- VERTICAL GRID FOR DEEP CONVECTION MODEL
HEIGHT OF VERTICAL LEVEL

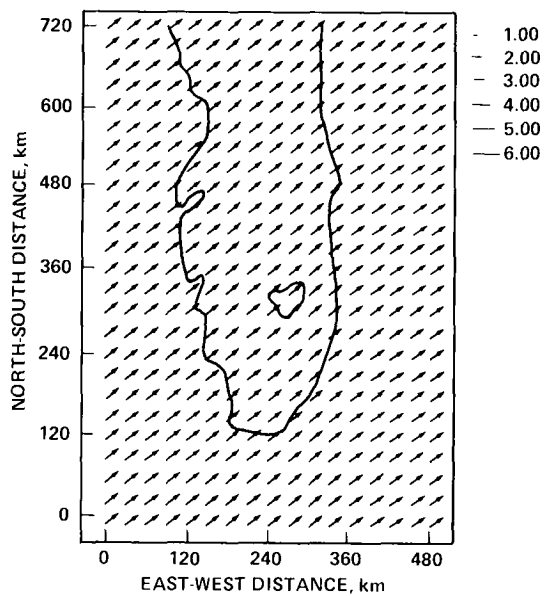
Level no.	Height, km
18	16.00
17	14.00
16	12.00
15	10.00
14	8.50
13	7.00
12	6.00
11	5.00
10	4.05
9	3.20
8	2.45
7	1.80
6	1.25
5	.80
4	.45
3	.20
2	.05
1	0

TABLE II.- COMPARATIVE CPU RATES AND STORAGE CAPACITIES

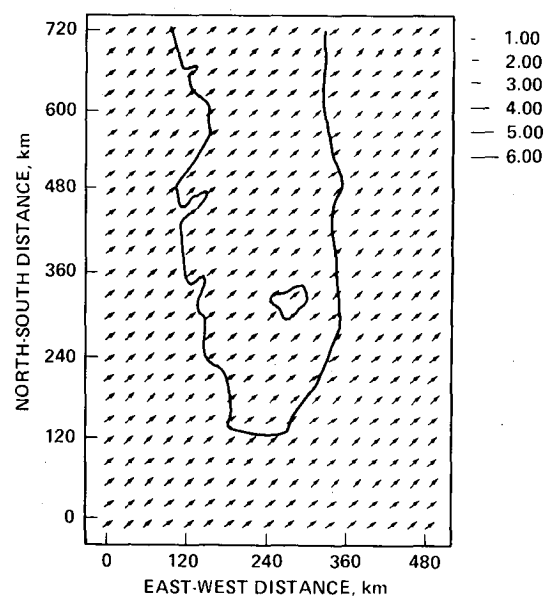
^a Amdahl-470V/6	^b CDC-6600	^b CDC STAR-100	^c CDC-7600	^c CRAY-1
CPU performance ratio				
1.0 to 1.33	0.37	2.59 to 24.89	1.85	3.7 to 14.8
2.7 to 3.6	1.0	7.00 to 67.2	5.0	10.0 to 40.0
0.39 to 0.51	0.14	1.00 to 9.6	0.71	1.43 to 5.71
0.04 to 0.05	0.01	0.10 to 1.0	0.07	0.11 to 0.42
0.54 to 0.72	0.2	1.4 to 13.44	1.0	2.0 to 8.0
0.27 to 0.36	0.1	0.7 to 6.72	0.5	1.0 to 4.0
0.03 to 0.09	0.03	0.175 to 1.68	0.13	0.25 to 1.0
CPU word storage capacity				
1 048 576 plus VM ^d	131 000	512 000 plus VM ^d	512 000	1 048 576

^aUniversity of Michigan.^bNASA Langley Research Center.^cNational Center for Atmospheric Research.^dVirtual memory.TABLE III.- CPU PERFORMANCE RATIOS FOR STAR-100/CDC-6600
IN RELATION TO NUMBER OF GRID POINTS

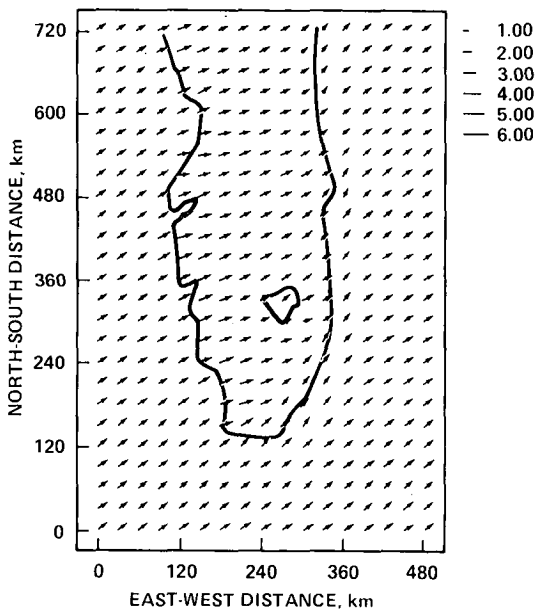
No. of grid points	CPU performance ratio STAR-100/CDC-6600
168	13.5
280	12.3
336	20.3
504	24.4
2800	67.2



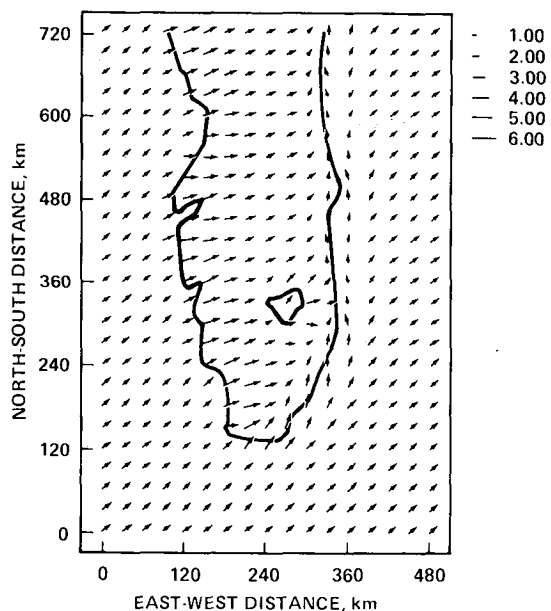
(a) After first hour.



(b) After second hour.

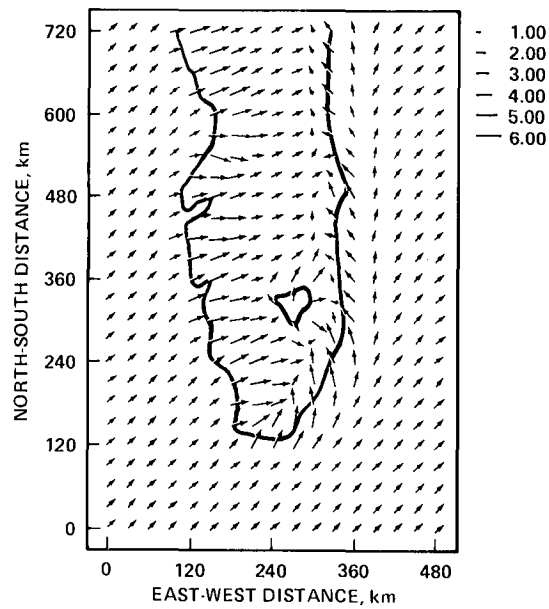


(c) After third hour.

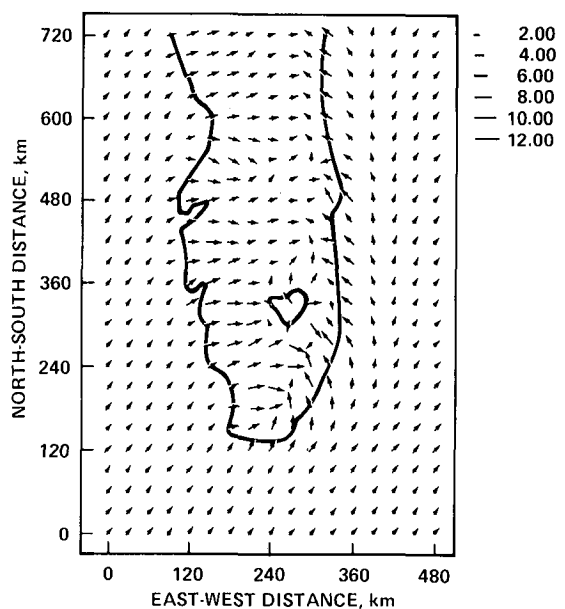


(d) After fourth hour.

Figure 1.- Horizontal wind field for various elapsed times at 50-meter level. Velocity vectors are in meters per second. (Conditions are as follows: undisturbed, neutral, and dry air; initial windspeed of 6 m/sec from southwest at all levels.)

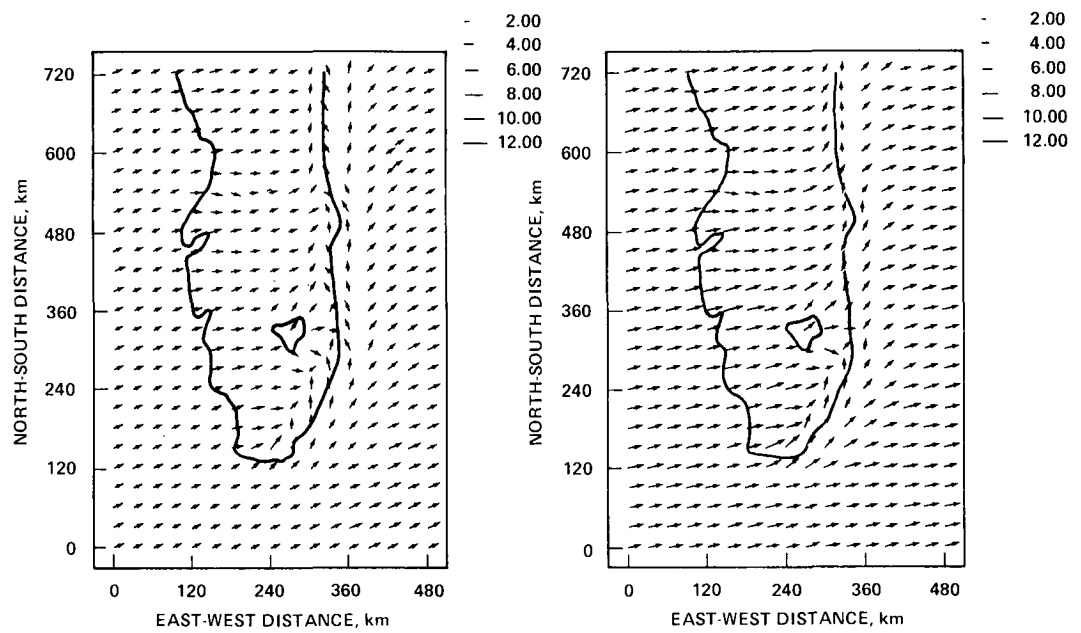


(e) After fifth hour.



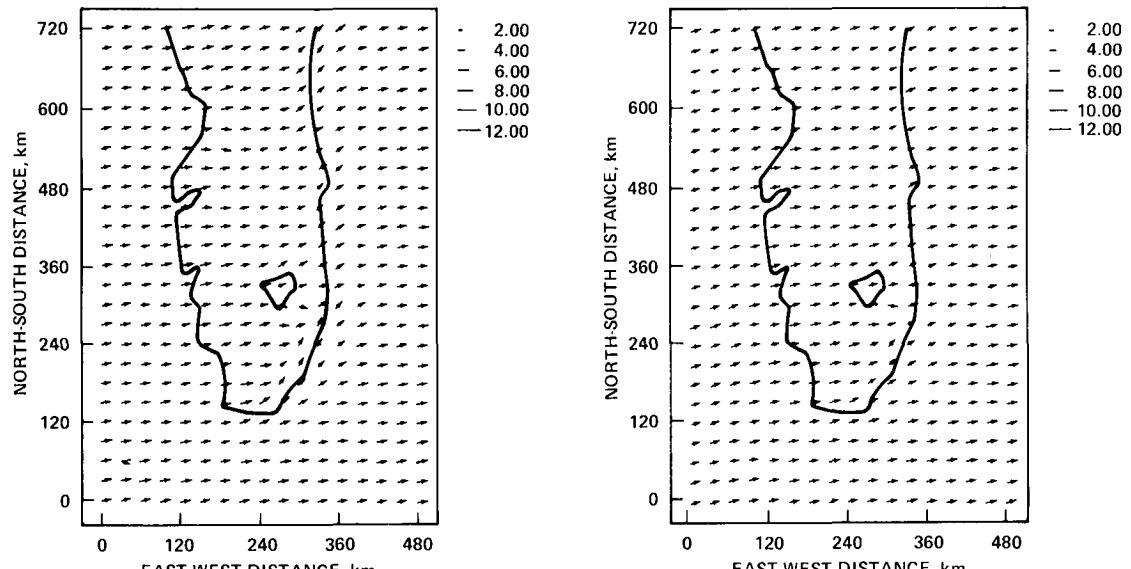
(f) After sixth hour.

Figure 1.- Concluded.



(a) At 200-meter level.

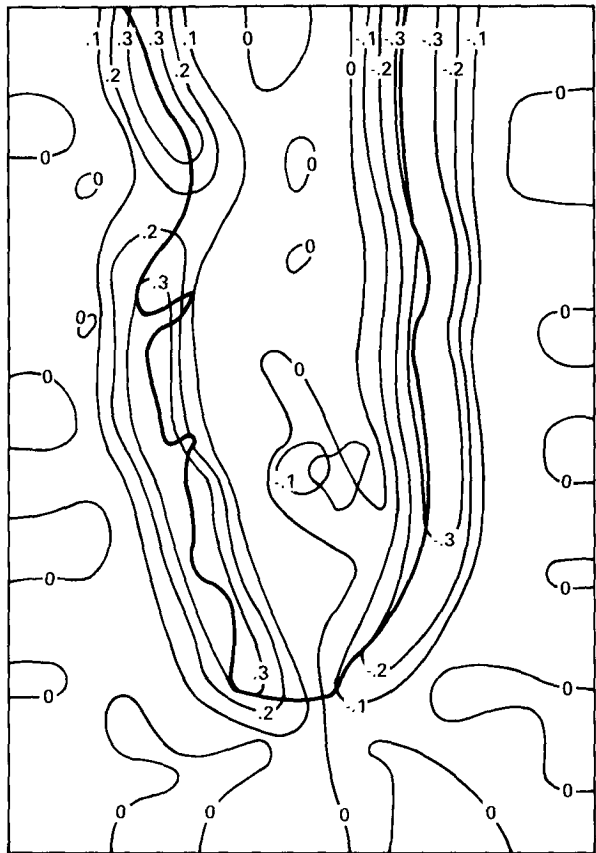
(b) At 450-meter level.



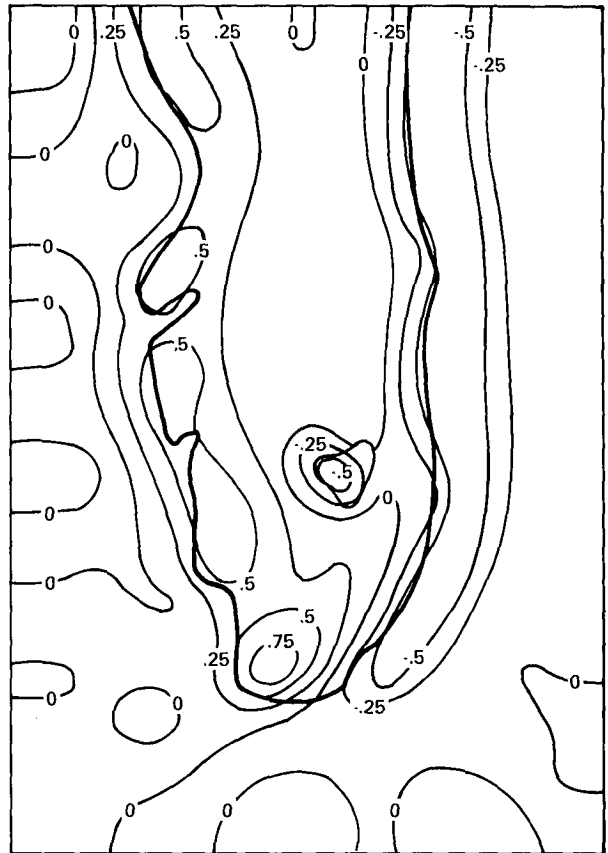
(c) At 800-meter level.

(d) At 1250-meter level.

Figure 2.- Horizontal wind field at various altitudes after sixth hour. Velocity vectors are in meters per second. (Conditions are the same as for fig. 1.)

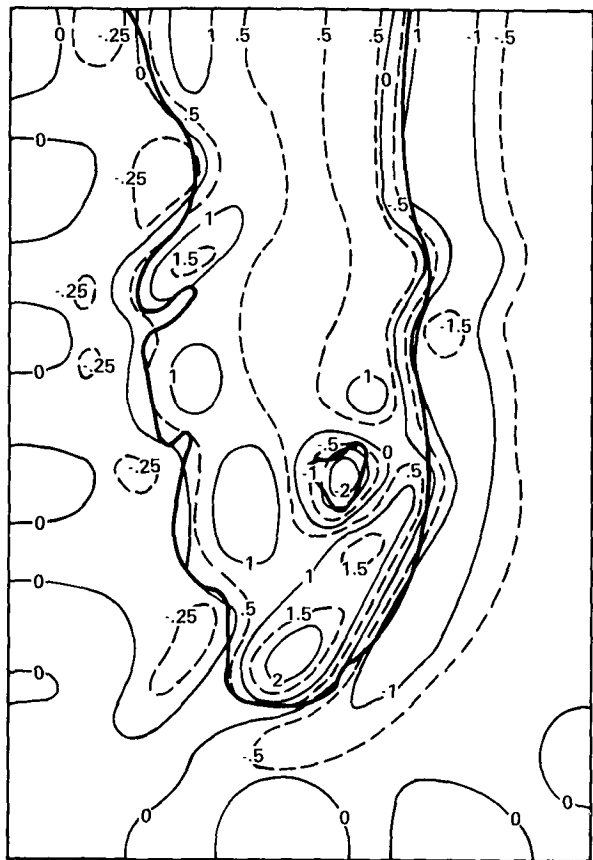


(a) After first hour.

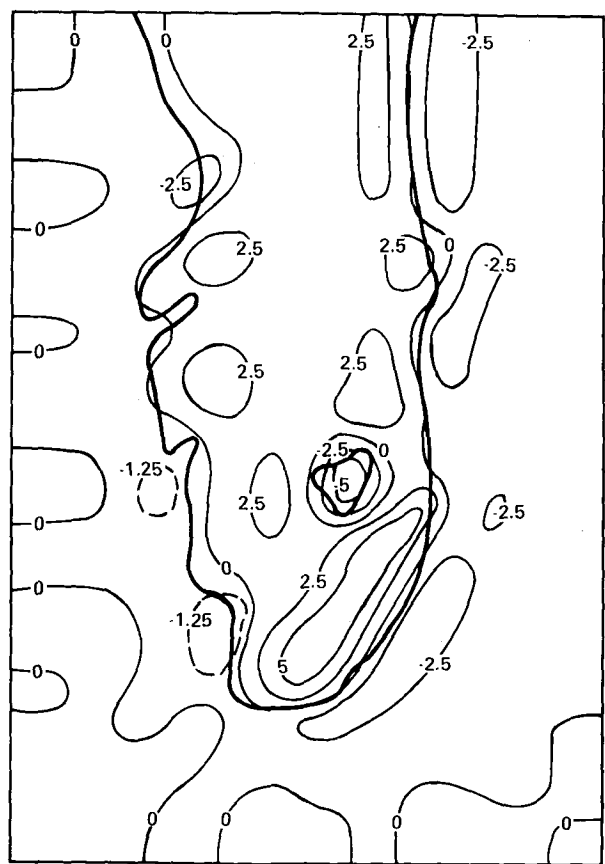


(b) After second hour.

Figure 3.- Distribution of vertical wind velocity (centimeters per second) for various elapsed times at 1250-meter level. (Conditions are the same as for fig. 1.)

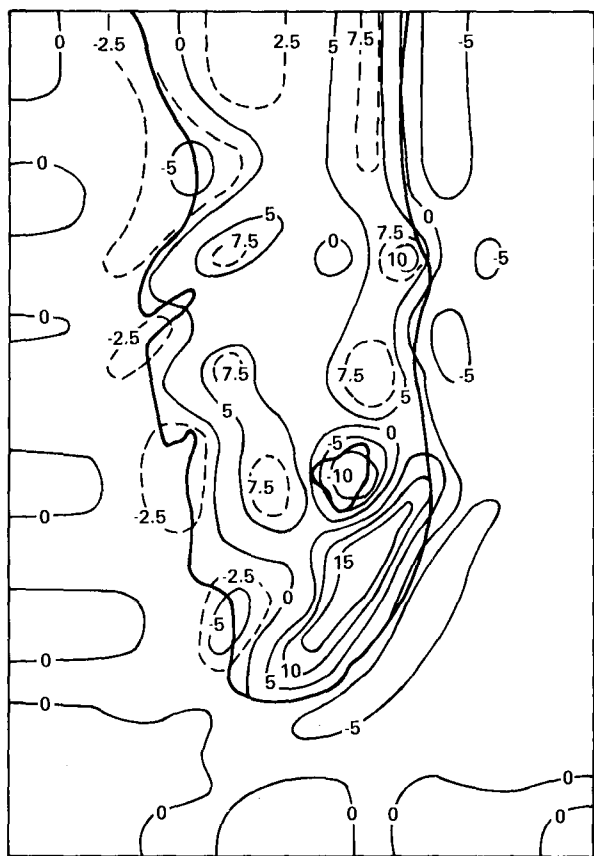


(c) After third hour.

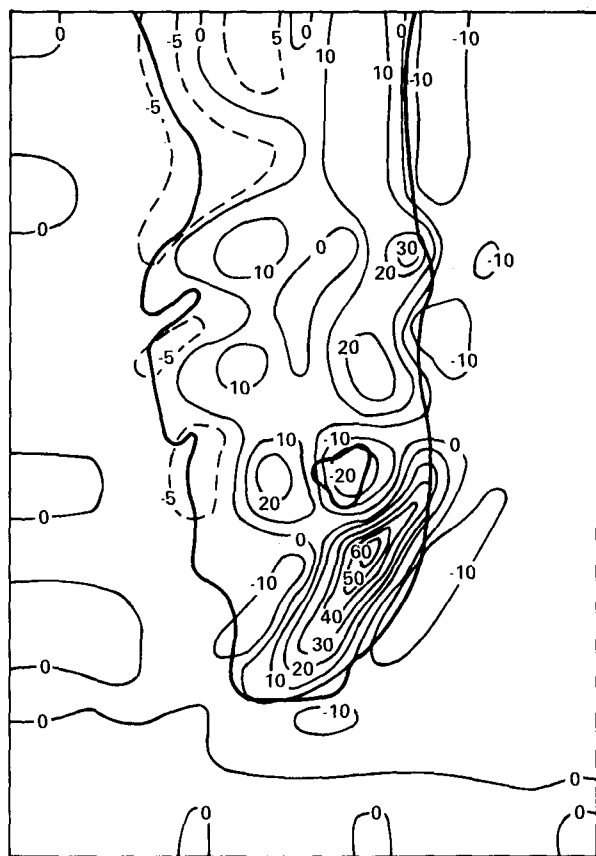


(d) After fourth hour.

Figure 3.- Continued.

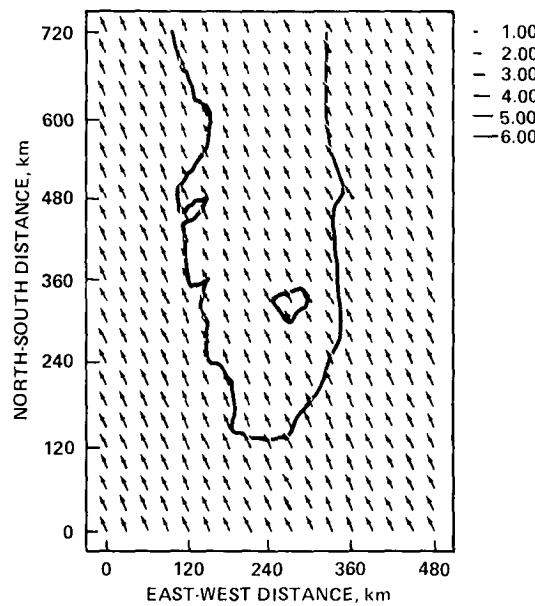


(e) After fifth hour.

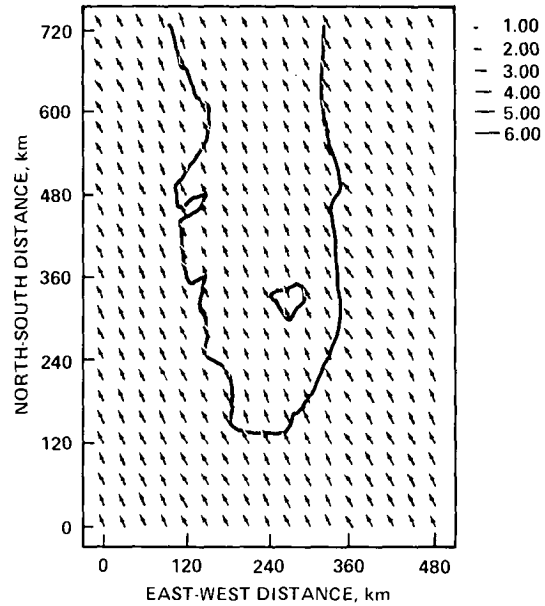


(f) After sixth hour.

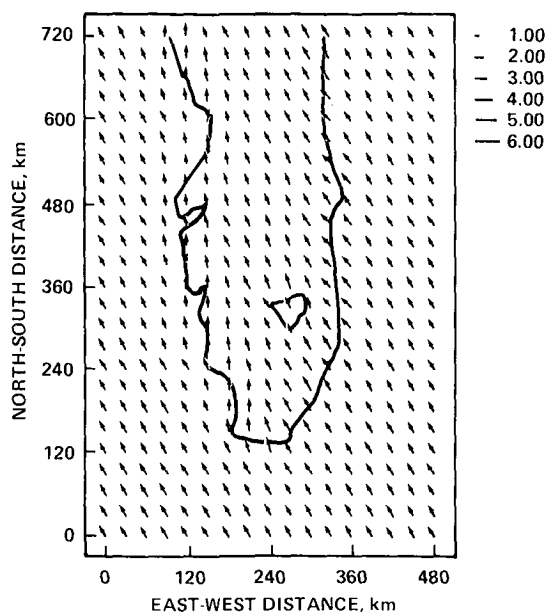
Figure 3.- Concluded.



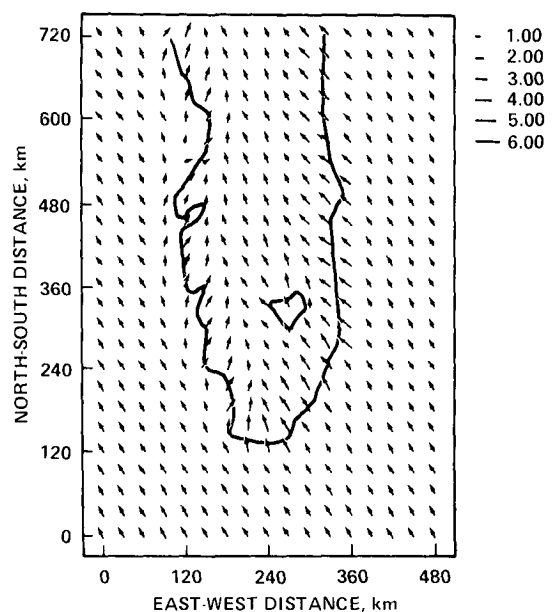
(a) After first hour.



(b) After second hour.

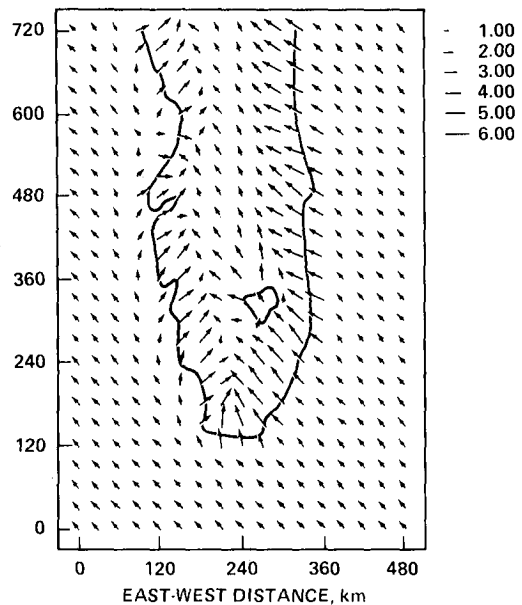


(c) After third hour.

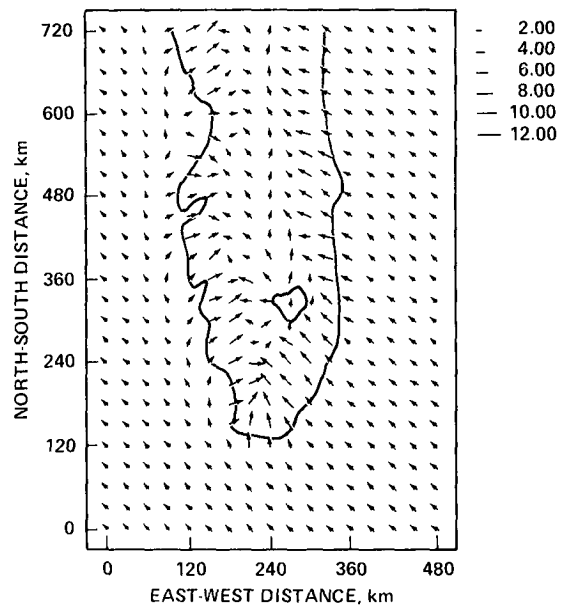


(d) After fourth hour.

Figure 4.- Horizontal wind field for various elapsed times at 50-meter level. Velocity vectors are in meters per second. (Conditions are as follows: undisturbed, neutral, and dry air; initial windspeed of 6 m/sec from southeast at all levels.)

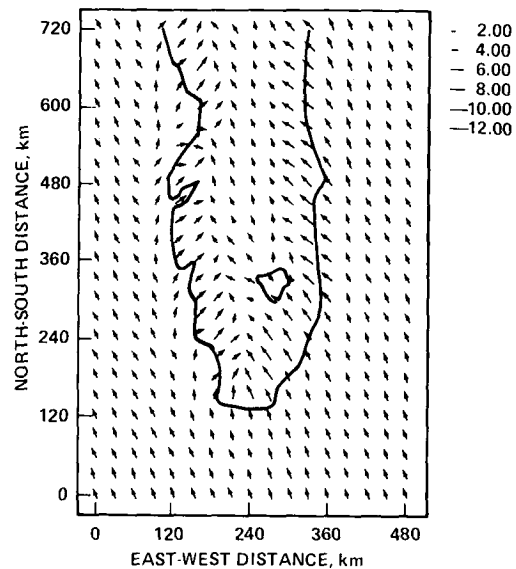


(e) After fifth hour.

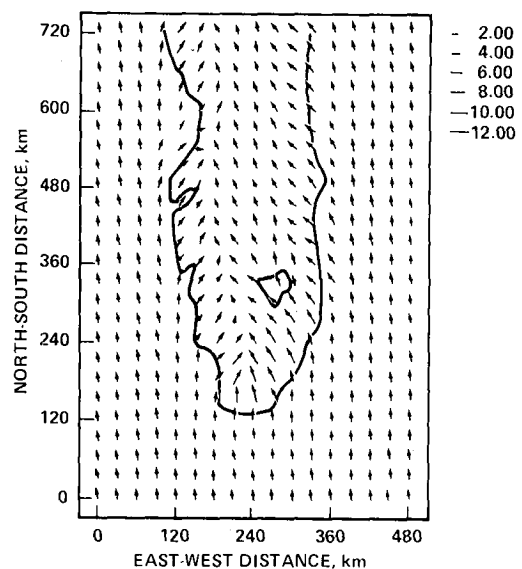


(f) After sixth hour.

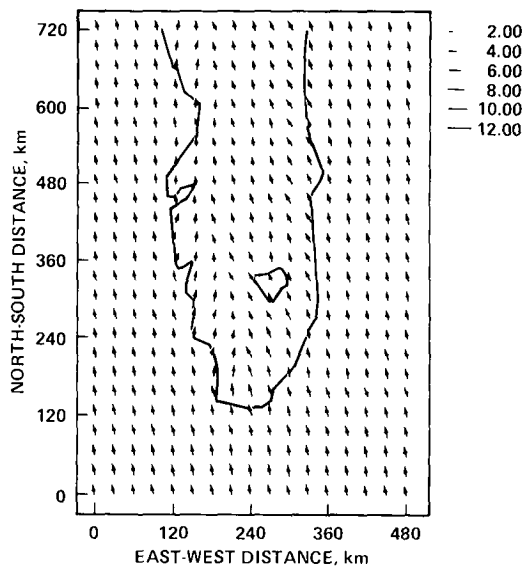
Figure 4.- Concluded.



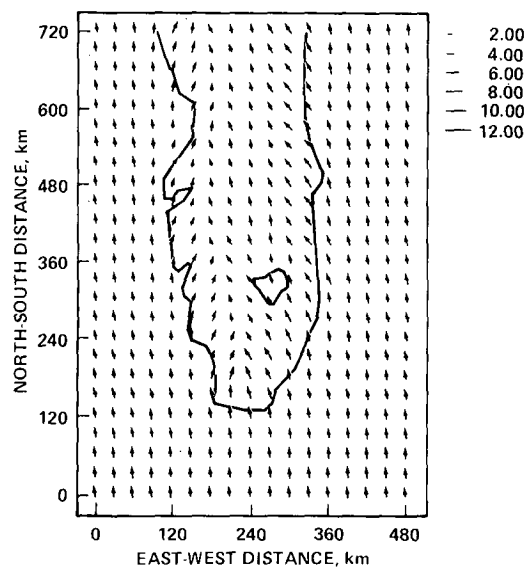
(a) At 200-meter level.



(b) At 450-meter level.



(c) At 800-meter level.

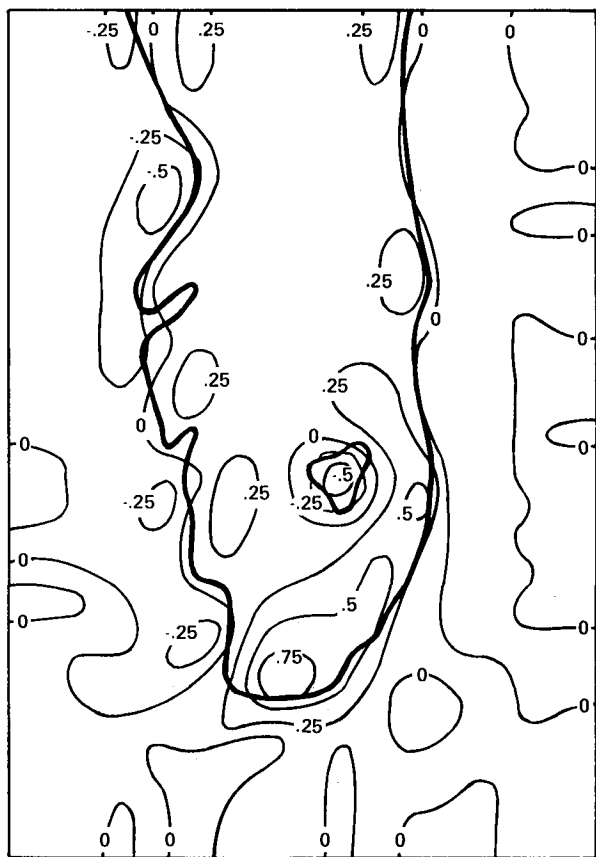


(d) At 1250-meter level.

Figure 5.- Horizontal wind field at various altitudes after sixth hour. Velocity vectors are in meters per second. (Conditions are the same as for fig. 4.)

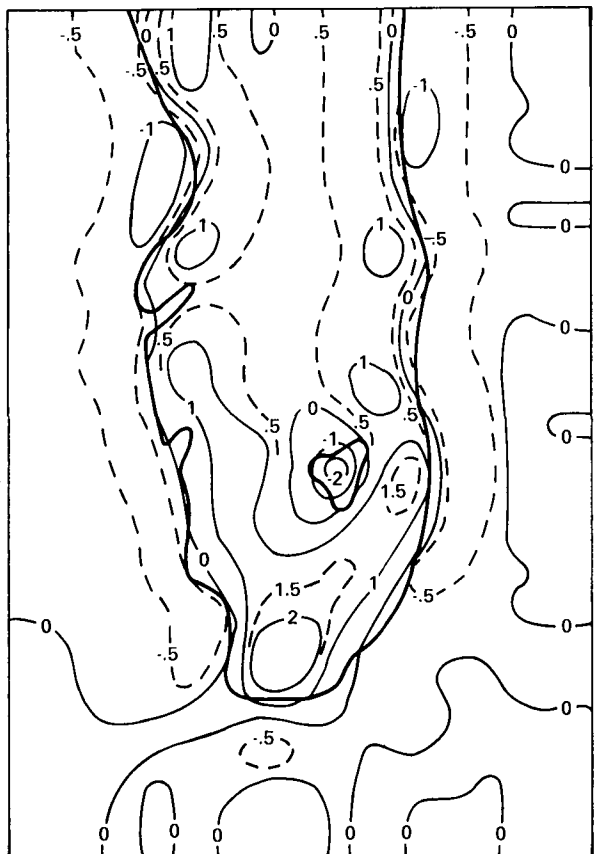


(a) After first hour.

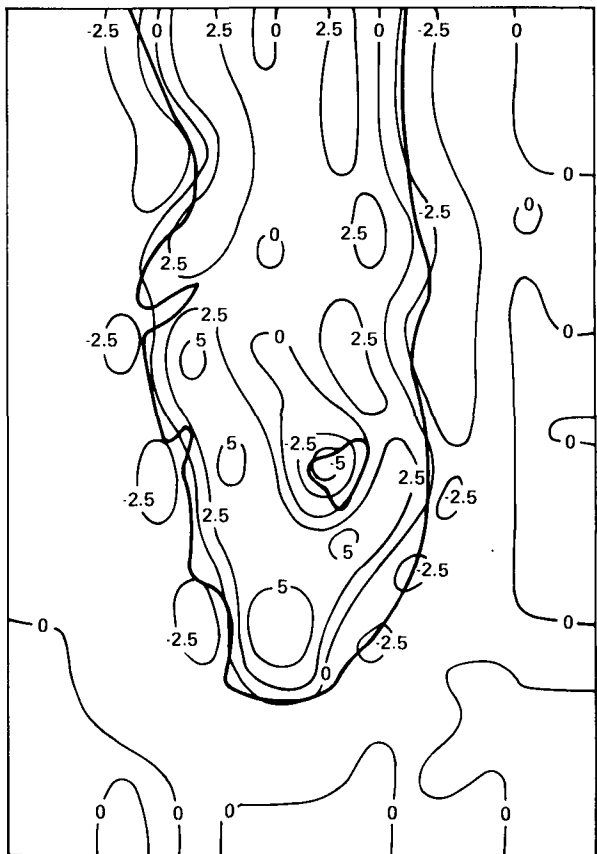


(b) After second hour.

Figure 6.- Distribution of vertical wind velocity (centimeters per second) for various elapsed times at 1250-meter level. (Conditions are the same as for fig. 4.)

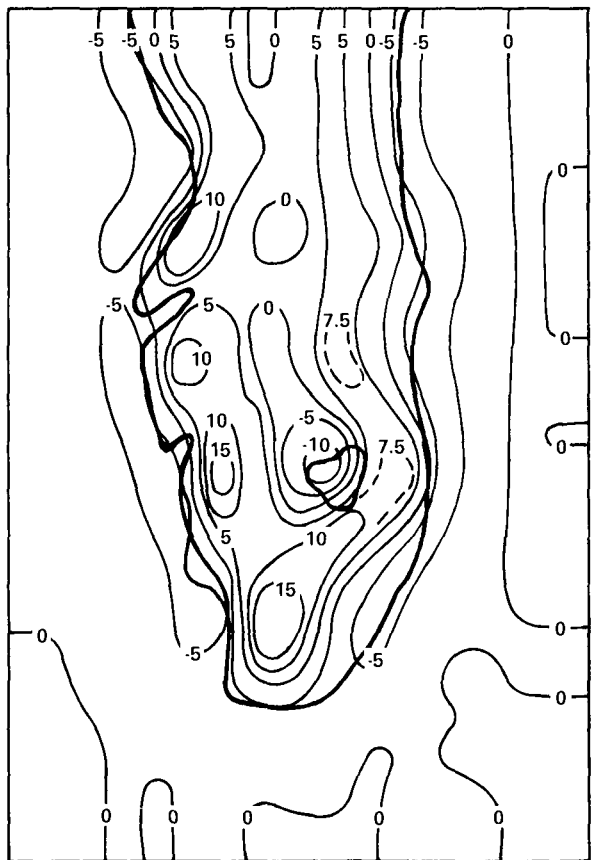


(c) After third hour.

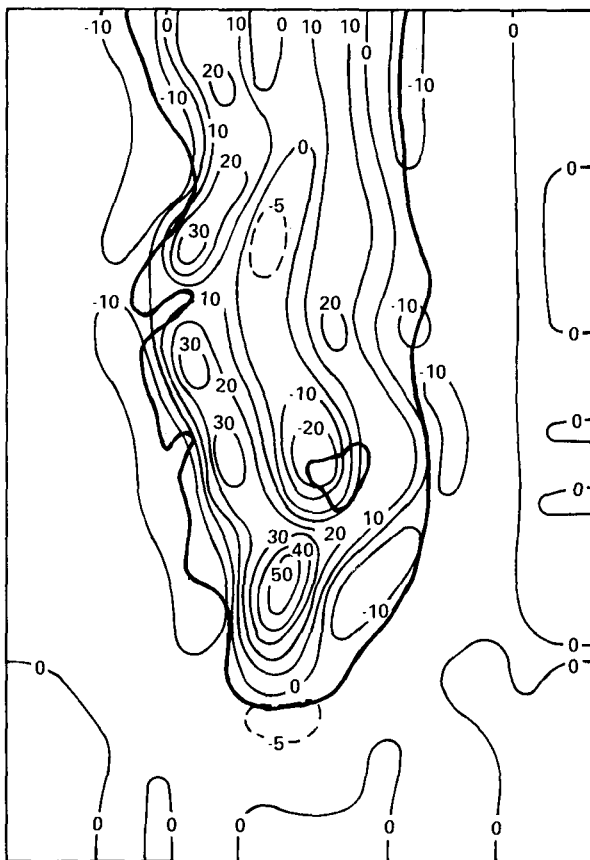


(d) After fourth hour.

Figure 6.- Continued.



(e) After fifth hour.



(f) After sixth hour.

Figure 6.- Concluded.

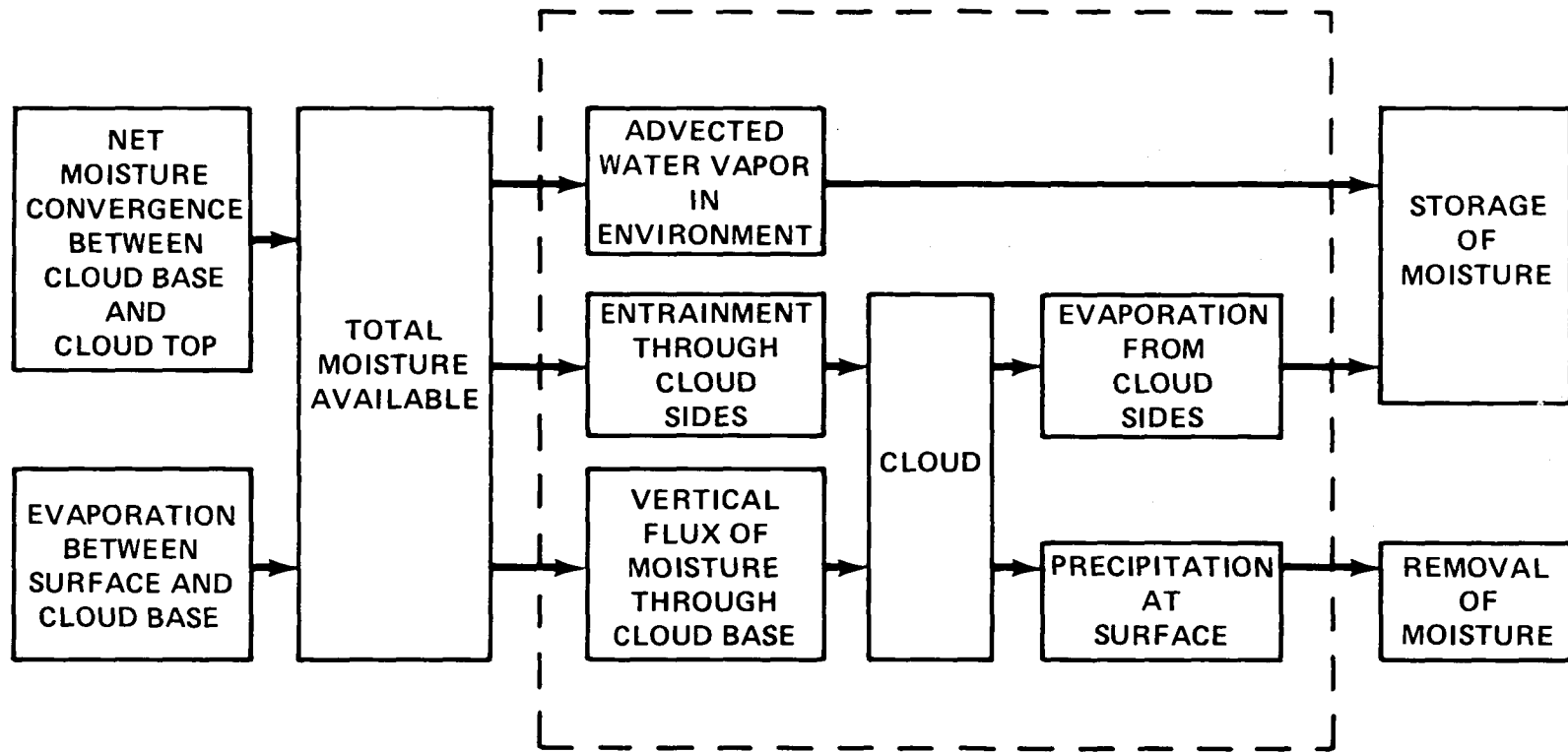


Figure 7.- Parameterization scheme for convective cloud and precipitation in the mesoscale model.

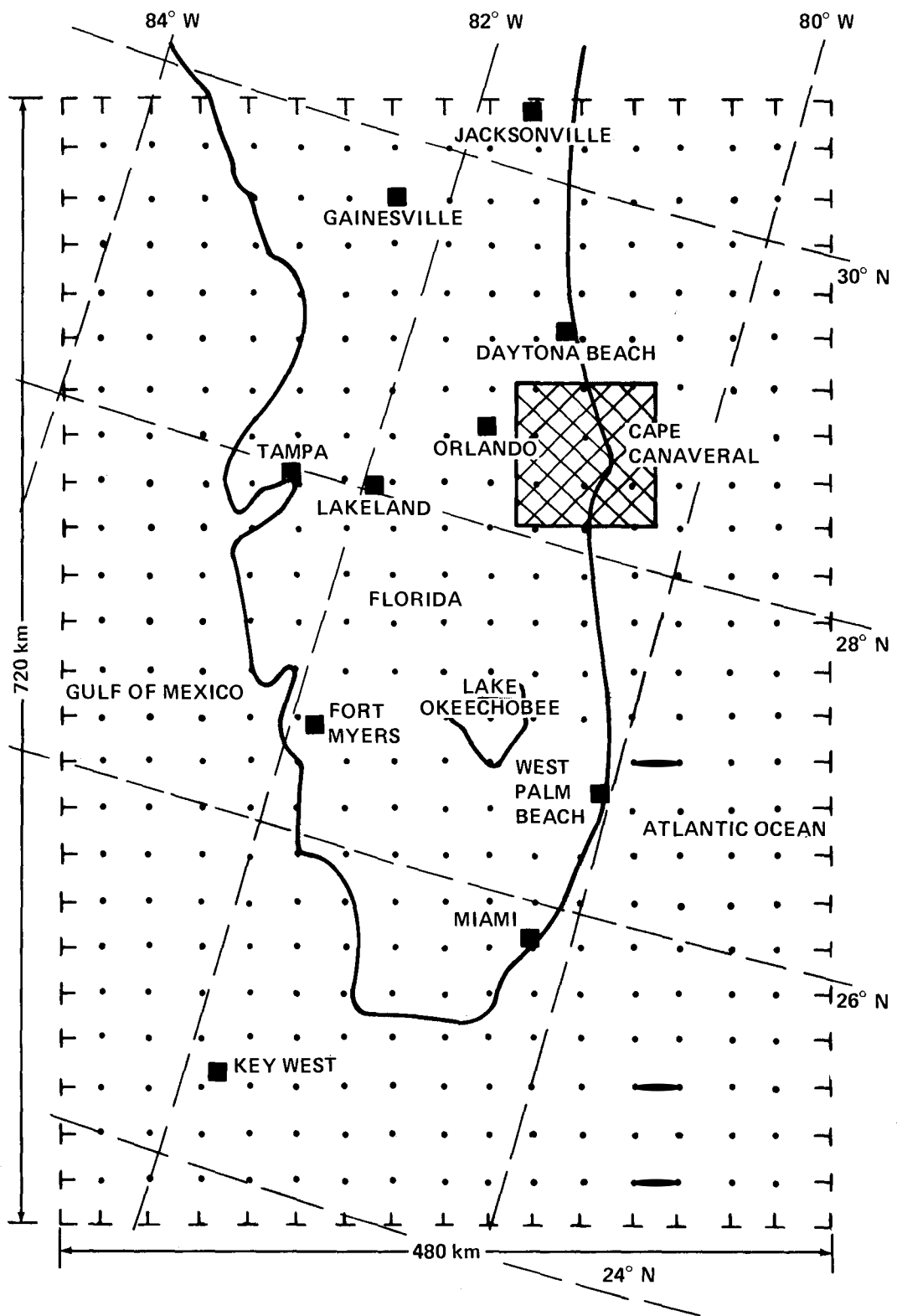


Figure 8.- Map showing the area to be covered by the submesoscale model.